



Journal Name

ARTICLE

Meta-analysis: the molecular organization of non-fullerene acceptors

Received 00th January 20xx,
Accepted 00th January 20xx

Pierluigi Mondelli,^a Gabriele Boschetto,^b Peter N. Horton,^c Priti Tiwana,^a Chris-Kriton Skylaris,^b Michal Krompiec^{a,b} and Graham Morse^{a*}

DOI: 10.1039/x0xx00000x

www.rsc.org/

The rapid development of non-fullerene acceptors (NFAs) for organic solar cells has recently pushed the Power Conversion Efficiencies (PCE) over the 15% threshold, surpassing fullerene-based state-of-the-art devices. However, for the commercialization of large-scale photovoltaic modules, thick active layers films (150–300 nm) with high PCE and fill factors are required. Thus, the realization of materials with higher charge mobilities is fundamental for the roll-to-roll printing industry, and therefore the understanding of the factors that are limiting for the charge transport properties of the NFAs becomes crucial for this strategy. The study of the molecular packing and arrangement of NFAs in the solid state provides direct insights about the propensity of the pristine materials to crystallize and contribute efficiently to the charge transport. In this work we combine experimental techniques and molecular modelling, with the aim of analyzing the way in which NFAs interact in the solid state and the key components of their structures for building efficient percolation pathways for charge transport. To this end, several new molecules were synthesized and crystallized by solvent vapour diffusion, which were then characterized by single crystal X-Ray Diffraction (XRD). These structures were further compared to a wide selection of literature materials. Density functional theory (DFT) calculations were also carried out to examine the electronic transport of these materials with respect to their molecular packing motifs.

Introduction

Organic Solar Cells (OSC) based on NFAs have been the focus of research since the inception of the field of Organic Photovoltaics (OPV).^{1–5} Recently, new designs proposed by Xiaowei Zhan⁶ has led to a surge in performance beyond 15% PCE,⁷ going far beyond the best fullerene-based OSCs.^{8,9} NFA molecules intrinsically possess many advantages over fullerenes, including a more efficient light absorption and tunability of the energy levels,^{3,10} leading to higher photocurrent and reduced voltage losses in the devices.¹¹ Despite the advantages, NFAs are still lagging behind fullerene acceptors in terms of charge transport properties.^{12,13} Therefore, low electron mobilities represent a major challenge for the commercialization of solution-processed fullerene-free OPV devices, which requires high performance in the thick-film active layer regime (150–300 nm), being the most realistic

window for common large-scale roll-to-roll printing techniques.¹⁴ The reason for the difference between these two classes of materials can be linked to their molecular shape, which in turn affects the molecular packing and the charge transport properties.^{15–18} Indeed, PC₆₁BM possesses a unique and beneficial feature for a fast charge transport: the near-ball-shaped molecular structure allows for formation of three-dimensional charge percolation network and at the same time ensures the typical domain sizes to be within the exciton diffusion length (~20 nm).¹² On the other hand, NFAs are characterised by highly anisotropic conjugated structures, and their two-dimensional geometry makes the molecular packing, domain orientation and blend morphology^{19,20} crucial for the electron mobility, charge separation and charge collection at the electrodes.^{21–23} Therefore, it is essential to study and understand the solid-state arrangement of NFA molecules to achieve better performing systems. Despite in many fields of organic electronics the influence of molecular packing on the charge transport properties have been extensively studied both theoretically and experimentally,^{15,16,24–26} in OPV this topic has started to draw the attention only recently.^{17,26–35} In this review, we explore the way in which these molecules interact in the solid state and how the chemical design can influence the molecular organization, focusing on a specific class of NFA materials: fused rings electron acceptors (FREA). These molecules are typically composed by linearly fused acceptor-donor-acceptor (A-D-A) aromatic backbones with the side chains located on sp³-hybridized carbon atoms near the centre

^a Merck Chemicals Ltd, Chilworth Technical Centre, University Parkway, Southampton SO16 7QD, UK. Email: graham.morse@merckgroup.com

^b School of Chemistry, University of Southampton, Highfield, Southampton, SO17 1BJ, UK

^c EPSRC Crystallographic Service, Department of Chemistry, University of Southampton, Highfield, SO17 1BJ, UK.

† Footnotes relating to the title and/or authors should appear here.

Electronic Supplementary Information (ESI) available: [details of any supplementary information available should be included here]. See DOI: 10.1039/x0xx00000x

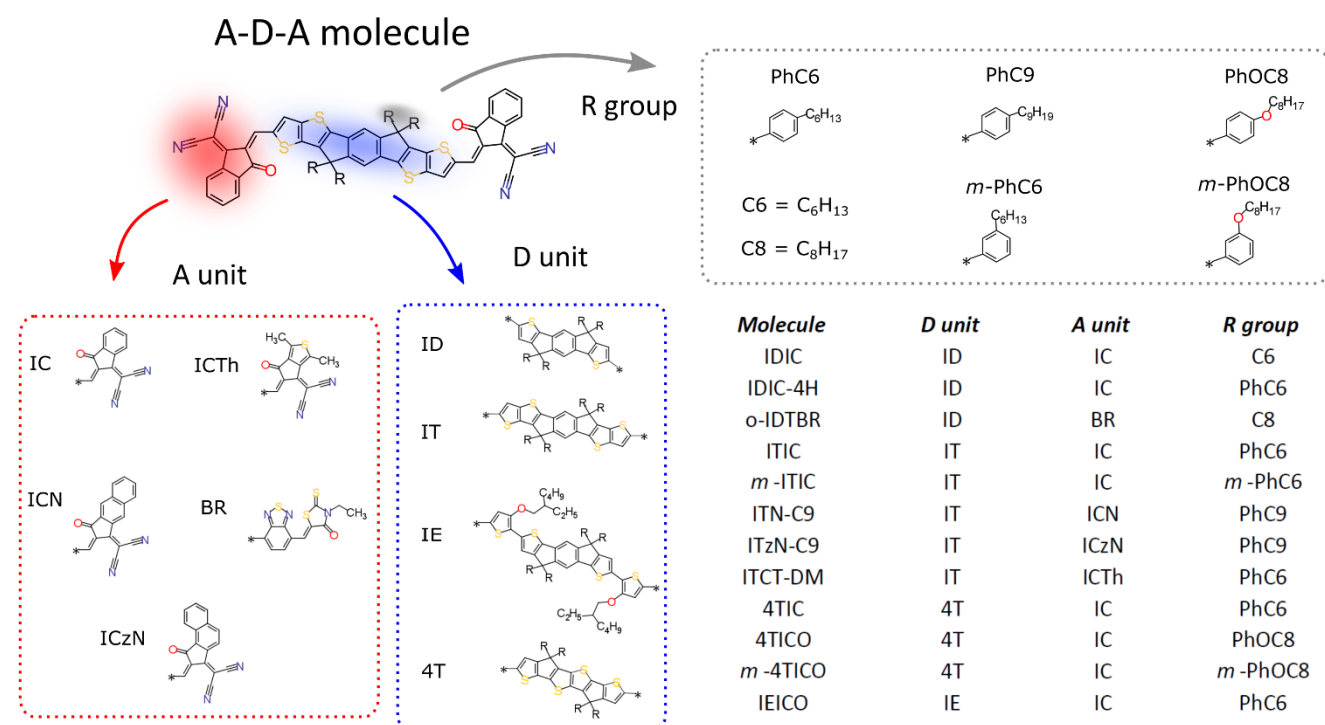


Figure 1 Chemical structure of the A-D-A family molecules with its building blocks.

of the molecule. Comparisons to related families of molecules such as small acceptor (D-A molecules) and donor molecules (D molecules) will be used to support and contrast our observations.

A meta-analysis of the molecular packing and the crystallization tendencies will be carried out over a wide selection of crystal structures known in literature and newly identified ones. The discussion will identify the most common features and trends related to molecular packing; considerations about packing motifs, density of packing and π - π interaction strength will highlight the influence of the molecular organization on the charge transport. To further discuss the importance that molecular packing and topological connectivity have on the charge transport properties, DFT calculations will be performed on a few A-D-A molecules to evaluate their electron effective masses. In particular, by comparing the effective masses values calculated along different directions for several structures, it will be possible to draw conclusions about the influence of the topological connectivity at the molecular level on the charge transport anisotropy.

Experimental

Crystal Growth

Single crystals suitable for XRD analysis were grown by solvent vapour diffusion: the compound of interest was dissolved and diffused in an antisolvent vapour (Table 1). For most of the crystal structures diffracted in this work, the use of petroleum ether 40-60 (PE₄₀₋₆₀) and chloroform have been successful with the only exception of the 4TICO molecule (chemical structure shown in Figure 1). All the solvents were purchased from Sigma Aldrich. 4TICO and m-4TICO molecules were synthesised following the procedure described in the related patent.³⁶ The chemical structures of IDT01 and ICA small molecules are shown in Figure 2), while the ICNA small molecule acceptor is equivalent to the "ICN" acceptor unit shown in Figure 1 with an alkyl side chain "C6". IEICO was purchased from Solarmer Material Inc (China) while ITIC, m-ITIC and IDIC from 1-Material (Canada). The synthetic routes for IEICO, m-ITIC, ITIC and IDIC are reported in literature.³⁷⁻⁴⁰

Table 1 Crystallographic information and growth conditions attempted to explore single crystal packing of the A-D-A molecules, small acceptor end groups and donor molecules. Literature samples are included.

CCDC identifier	Compound name	solvent/anti- solvent	Crystallization Precipitate	Crystal System	Space Group	Solvate inclusions	φ (%) ^a	φ_s (%) ^b	Motif	π - π stacking g ^c
A-D-A molecules										
KIZSUK ⁴¹	ITIC	CHCl ₃ /PE ₄₀₋₆₀	crystalline	triclinic	$P\bar{1}$	none	35.51	-	herringbone	0D
	ITIC	CHCl ₃ /C ₂ H ₅ OH	amorphous solid	-	-	-	-	-	-	-
	ITIC	CHCl ₃ /CH ₃ OH	crystalline ^e	-	-	-	-	-	-	-
	ITIC	C ₆ H ₅ Cl/C ₆ H ₁₂	molecular glass	-	-	-	-	-	-	-
	ITIC	CHCl ₃ /C ₃ H ₆ O	amorphous solid	-	-	-	-	-	-	-
	ITIC	CH ₂ Br ₂ /C ₇ H ₁₆	crystalline	triclinic	$P\bar{1}$	CH ₂ Br ₂	-	-	brickwork	2D
	4TICO	CHCl ₃ /PE ₄₀₋₆₀	crystalline ^e	-	-	-	-	-	-	-
	4TICO	CHCl ₃ /C ₂ H ₅ OH	crystalline ^e	-	-	-	-	-	-	-
	4TICO	CHCl ₃ /CH ₃ OH	crystalline ^e	-	-	-	-	-	-	-
	4TICO	C ₆ H ₅ Cl/C ₆ H ₁₂	crystalline ^e	-	-	-	-	-	-	-
	4TICO	CHCl ₃ /C ₃ H ₆ O	crystalline	monoclinic	P2 ₁ /c	C ₃ H ₆ O	34.61	36.67	herringbone	0D
	m-4TICO	CHCl ₃ /PE ₄₀₋₆₀	crystalline	triclinic	$P\bar{1}$	CHCl ₃	33.82	39.25	brickwork	2D
	m-4TICO	CHCl ₃ /CH ₃ OH	crystalline ^f	-	-	-	-	-	-	-
	m-ITIC	CHCl ₃ /PE ₄₀₋₆₀	crystalline	triclinic	$P\bar{1}$	CHCl ₃	35.11	38.15	brickwork	2D
	m-ITIC	CHCl ₃ /CH ₃ OH	molecular glass	-	-	-	-	-	-	-
	IEICO	CHCl ₃ /PE ₄₀₋₆₀	crystalline	monoclinic	C2/c	CHCl ₃	37.43	42.1	reticular	3D
	IEICO	CHCl ₃ /CH ₃ OH	crystalline ^e	-	-	-	-	-	-	-
	IDIC	CHCl ₃ /PE ₄₀₋₆₀	crystalline	triclinic	$P\bar{1}$	none	34.79	-	brickwork	2D
IDIC	CHCl ₃ /CH ₃ OH	crystalline ^f	-	-	-	-	-	-	-	
IDIC	C ₆ H ₅ Cl/C ₆ H ₁₂	crystalline ^f	-	-	-	-	-	-	-	
IDIC	CHCl ₃ /C ₃ H ₆ O	crystalline ^f	-	-	-	-	-	-	-	
YEBKEY ⁴²	4TIC	C ₇ H ₈ / CH ₃ OH	crystalline	triclinic	$P\bar{1}$	both ^g	-	-	reticular	3D
1889754	o-IDTBR	Unknown	crystalline	monoclinic	P2 ₁ /c	none	36.03	-	reticular	3D
KIQVOY ²⁸	ITCT-DM	Unknown	crystalline	monoclinic	C2/c	none	36.30	-	reticular	3D
ZIHBW ³¹	ITN-C9	CH ₂ Br ₂ /C ₃ H ₆ O	crystalline	triclinic	$P\bar{1}$	CH ₂ Br ₂	35.3	47.32	brickwork	2D
ZIHBEA ³¹	ITzN-C9	CH ₂ Br ₂ /C ₃ H ₆ O	crystalline	triclinic	$P\bar{1}$	CH ₂ Br ₂	-	-	brickwork	2D
YISJIW ³³	IDIC-4H	CHCl ₃ /C ₂ H ₅ OH	crystalline	triclinic	$P\bar{1}$	none	35.36	-	brickwork	2D
Small acceptor molecules - D - A molecules										
SAHZEI ⁴³	ICA	CHCl ₃ /PE ₄₀₋₆₀	crystalline	triclinic	$P\bar{1}$	none	31.36	-	slip-stacked	1D
	ICA	CHCl ₃ /CH ₃ OH	crystalline ^e	-	-	-	-	-	-	-
	ICNA	CHCl ₃ /PE ₄₀₋₆₀	crystalline	monoclinic	P2 ₁ /n	none	29.19	-	herringbone*	1D
	ICNA	CHCl ₃ /CH ₃ OH	molecular glass	-	-	-	-	-	-	-
BUXYEA ⁴⁴	n/a	Unknown	crystalline	triclinic	$P\bar{1}$	none	33.29	-	slip-stacked	1D
HEHYAW ⁴⁵	n/a	unknown	crystalline	monoclinic	P2 ₁ /c	none	29.76	-	lamellar	1D
BUXYAW ⁴⁴	n/a	unknown	crystalline	triclinic	$P\bar{1}$	none	33.91	-	slip-stacked	1D
Small donor molecules - D molecules										
QEGHAO ⁴⁶	IDT01	Unknown	crystalline	triclinic	$P\bar{1}$	none	35.23	-	herringbone*	1D
	PDT	CH ₂ Cl ₂ /C ₄ H ₈ O ₂	crystalline	triclinic	$P\bar{1}$	none	35.52	-	slip-stacked	1D
	SITJOW ⁴⁷	n/a	CH ₂ Cl ₂ /CH ₃ CN	monoclinic	P2 ₁ /c	none	34.24	-	herringbone	0D
	SITJUC ⁴⁷	n/a	CH ₂ Cl ₂ /CH ₃ CN	monoclinic	P2 ₁ /c	none	33.83	-	herringbone*	1D
SIGMON ⁴⁸	n/a	CHCl ₃ /CH ₃ OH	crystalline	triclinic	$P\bar{1}$	none	37.22	-	slip-stacked	1D
SERVOB ⁴⁹	n/a	Unknown	crystalline	triclinic	$P\bar{1}$	CHCl ₃	N/A	-	slip-stacked	1D

WEHNEF ⁵⁰	n/a	CHCl ₃ /C ₂ H ₆ OS	crystalline	triclinic	$\bar{P}1$	both ^g	45.83	61.08	slip-stacked	1D
SITKAJ ⁴⁷	n/a	CH ₂ Cl ₂ /CH ₃ CN	crystalline	monoclinic	P2 ₁ /n	none	35.65	-	herringbone	0D
SITLEO ⁴⁷	n/a	CD ₂ Cl ₂ ^d	crystalline	triclinic	$\bar{P}1$	none	34.01	-	slip-stacked	1D
OFUPEN ⁵¹	DMIDT	Unknown	crystalline	triclinic	$\bar{P}1$	none	39.41	-	herringbone	0D
OFUPIR ⁵¹	IDT	Unknown	crystalline	triclinic	$\bar{P}1$	none	40.42	-	herringbone*	1D

^a Void fraction of solvent-masked and/or excessively disordered structures have been omitted for consistency. ^b Void fraction calculated when the solvent contribution is ignored. ^c Only cofacial alignment between aromatic rings has been considered. ^d Crystal grown by slow evaporation. ^e Crystallites size too small to be diffracted. ^f Non-diffracted crystal, another sample of the same molecule was chosen as more suitable for diffraction. ^g Both solvent and antisolvent molecules have been found in the crystal structure.

DFT calculations

Computer simulations were performed within the linear-scaling density functional theory (LS-DFT) framework, using the ONETEP code (Order-N Electronic Total Energy Package).⁵² In this approach, DFT can be expressed in terms of the density matrix $\rho(\mathbf{r}, \mathbf{r}')$, which in the Kohn-Sham formalism, is defined as

$$\rho(\mathbf{r}, \mathbf{r}') = \sum_i f_i \psi_i(\mathbf{r}) \psi_i^*(\mathbf{r}'),$$

where f_i is the occupancy of the state $\psi_i(\mathbf{r})$, effectively a Kohn-Sham orbital function. ONETEP relies on the density-matrix DFT formalism, however, $\rho(\mathbf{r}, \mathbf{r}')$ is expressed in terms of localized atom-centred orbital functions known as nonorthogonal generalized Wannier functions (NGWFs),⁵³ leading to

$$\rho(\mathbf{r}, \mathbf{r}') = \sum_{ab} \phi_a(\mathbf{r}) K^{ab} \phi_b^*(\mathbf{r}').$$

In the above expression, $\phi_a(\mathbf{r})$ and $\phi_b(\mathbf{r})$ are the NGWFs and K is known as the density kernel. By expanding the NGWFs in a basis of periodic sinc (psinc) functions,⁵⁴ the code conveniently relies on a plane-wave basis. ONETEP can achieve linear-scaling behaviour while maintaining at the same time near-complete basis set accuracy: linear-scaling computational cost is obtained by enforcing strict localization of the NGWFs and by truncation of the density kernel K via a spatial cut-off, which makes the density matrix sparse; plane-wave accuracy is achieved through the self-consistent optimization of both the density kernel and the NGWFs during calculations.

Calculation set-up

DFT calculations were performed on A-D-A like NFA crystal structures ranging from 468 to 1120 atoms. The atomic coordinates of published structures were taken from the Cambridge Crystallographic Data Centre (CCDC) database, whereas for the other structures the X-ray data was obtained in this work. X-ray data of o-IDTBR was kindly provided by Sarah Holliday.⁵⁵ For each NFA crystal, a DFT geometry optimization was performed on the hydrogen atoms only, since it is well known that X-ray diffraction does not provide reliable atomic coordinates for these. The atomic positions of C, O, S, N, the lattice vectors, and the cell angles were kept fixed, in order for the simulations to be performed on experimental data only. This set of simulations was carried out using the Perdew-Burke-Ernzerhof (PBE)⁵⁶ GGA exchange-correlation functional in conjunction with the projector augmented wave (PAW) method,⁵⁷ and with the inclusion of the D2 correction by

Grimme⁵⁸ to model dispersion interactions. A psinc kinetic energy cutoff of 800 eV was used, and the NGWFs radius for each atom species was set to 9.0 bohr. The number of NGWFs used was 4 NGWFs per C, N, O, S atom, and one NGWF per H atom. All ONETEP calculations were performed at the Γ point only.

Band structure calculations were performed at the PBE-D2 level using an interpolative approach as implemented in the ONETEP code.⁵⁹ For this method, it is necessary for the NGWF diameters to be less than half each lattice vector, and therefore for each structure the unit cell was doubled along the shortest vectors. Norm-conserving pseudopotentials were used to model core electrons, the kinetic energy cutoff was set to 800 eV. For reasons of computational efficiency the NGWF radii were set to 6.5 bohr - these settings ensured minimal changes (of the order of 0.02 eV) in the DFT bandgaps, as compared to the 9.0 bohr radii. For each crystal, the global minimum of the conduction band was located by sampling the Brillouin zone along the k-point paths suggested by Hinuma et al.⁶⁰ From the aforementioned calculations, the effective masses of electrons, which at a given k point and along a specific direction can be expressed as:

$$\frac{1}{m^*} = \frac{1}{\hbar^2} \left. \frac{\partial^2 E(k)}{\partial k^2} \right|_{k=k_0},$$

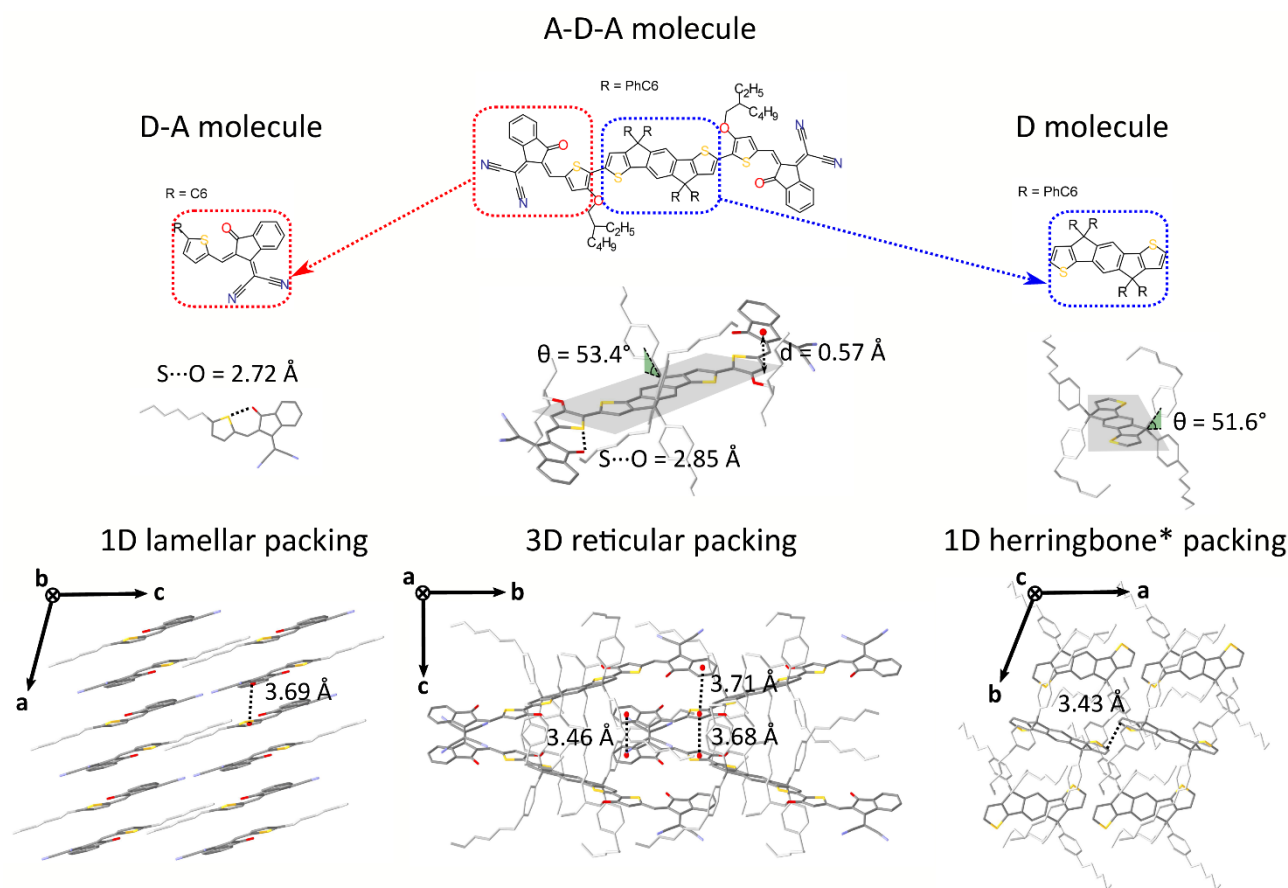


Figure 2 Chemical structures of IEICO (center) and its subunits: D-A small molecule "ICA" (left) and D molecule "IDT" (right) small donor molecule. b) Molecular conformations of ICA, IEICO and IDT small molecule in single crystal and representation of the dihedral angle θ between the side chains and the planar backbone and of the S...O conformational locks. c) Molecular packing representations for the three structures: 1D π - π lamellar stacking (ICA), reticular arrangement with a 3D π - π connectivity (IEICO) and herringbone motif with no π - π overlap (IDT).

were obtained by second-order polynomial interpolation of the bands performed at the conduction minimum.

X-Ray Diffraction

For all samples except IDT01, a suitable crystal was selected and mounted on a MITIGEN holder in oil on a Rigaku 007HF diffractometer equipped with Varimax confocal mirrors and an AFC11 goniometer and HyPix 6000 detector. The crystals were kept at $T = 100$ K during data collection. Data were measured using profile data from ω -scans using Cu- K_{α} radiation ($\lambda = 1.54178$ Å). Cell determination, data collection, data reduction, cell refinement and absorption correction were carried out using CrystalisPro.⁶¹

Sample IDT01 was run on a Nonius Kappa CCD diffractometer with Mo- K_{α} radiation ($\lambda = 0.71073$ Å) controlled by the Collect⁶² software package at 120(2) K. The data were processed using Denzo⁶³ and semi-empirical absorption corrections were applied using SADABS.⁶⁴

Using Olex²⁶⁵, all the structures were solved with the ShelXT⁶⁶ structure solution program and the models were refined with version 2018/3 of ShelXL⁶⁶ using Least Squares minimisation. All non-hydrogen atoms were refined anisotropically. Hydrogen

atom positions were calculated geometrically and refined using the riding model.

For samples 4TICO, m-ITIC and IEICO, the quality of crystals was such that they only prove gross connectivity. In general the core of these structures solved well, but there were issues especially with included solvent and external alkyl chains for which some were highly disordered. As such various geometrical (SADI, DFIX, BUMP) and displacement (RIGU, SIMU) restraints were used.

Results and Discussion

Molecular considerations

Molecular packing is, to a large extent, determined by intermolecular interactions.^{67, 68} For this reason, a common way of identifying the different packing motifs is by highlighting the dimensionality of the cofacial π - π overlap,^{24, 25, 69, 70} which is commonly believed to be providing an efficient electronic coupling between adjacent planar organic molecules. According to literature, the most recurrent motifs in organic semiconductor crystals are:

1. Herringbone packing with no extended (0D) π - π stacking (e.g. pentacene⁷¹),

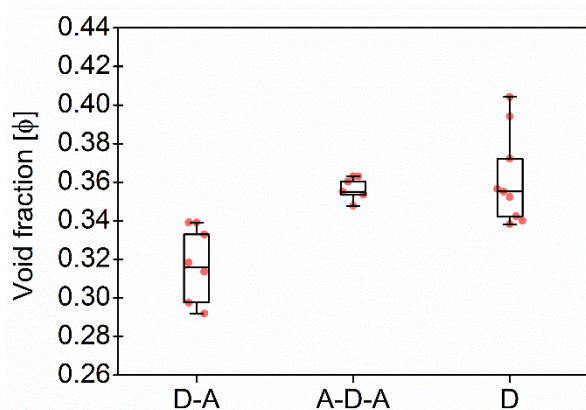


Figure 3 Calculated void fractions ϕ for the three family molecules studied in this work and listed in Table 1. The box plot denotes median (centre line), 25th quartile (bottom edge of the box), 75th quartile (top edge of the box), maximum and minimum values. Only non-solvated structures have been considered.

2. Non-classic herringbone with reduced one-dimensional (1D) π - π stacking (e.g. rubrene⁷²),
3. Lamellar/slip-stack packing with one-dimensional (1D) π - π overlap (e.g. 1,2,3,4-tetrafluoroanthracene⁷³), and
4. Brickwork with two-dimensional (2D) π - π stacking (e.g. TIPS-pentacene¹⁶).

Generally speaking, flat aromatic molecules would lead to 0D herringbone or 1D lamellar structures, as a result of the electrostatic repulsion between electron rich groups or dipole-dipole attraction between polar units.⁷⁰ A-D-A are similarly flat aromatic molecules with a more or less pronounced dipole character (due to the simultaneous presence of electron-rich and electron-poor units), however their central core contains sidechains which protrude out-of-plane and act to frustrate the 1D co-facial π -stacking. This frustration leads to the formation of more complex packing motifs: a reticular architecture with 3D π - π stacking (IEICO packing, Figure 2 and Figure 5) has been identified to be a common molecular arrangement amongst the ensemble of A-D-A molecules analysed in this work (Table 1, first section).

The most prolific molecular designs for A-D-A NFAs commonly consist of two acceptor groups such as indene malononitrile (IC) or rhodanine derivatives (BR), flanking a central donor core such as indacenodithiophene (ID) and indacenodithieno[3,2-b]thiophene (IT) (Figure 1). Researchers have been attempting to replace fullerene acceptors for over three decades, so this begs the question:

what makes recent acceptor-donor-acceptor NFAs so unique?

To support these design cues, the organization and the density of packing within the solid state of A-D-A molecules were compared to small molecule donor (D molecules) and D-A small molecules (Table 1 and Figure 2). An effective measure of the density of molecular packing in the unit cell is the void fraction (ϕ , as a percentage). This parameter has been used previously in order to compare the density of packing for different molecules, since it does not bias molecular size or weight.⁷⁴ A very simple chemical design as for the D-A small molecules (composed of a few aromatic rings with small and linear

sidechains) leads to the formation of molecules with high degree of planarity. All these structures have a high tendency of forming dense 1D packing motifs also due to their polar character, as they show the lowest values of void fraction (Figure 4) among the three families of molecules. As a result, a collection of crystal structures of flat aromatic donor-acceptor (D-A) molecules are characterized by lamellar, slip-stacked or herringbone structures with 1D co-facial π -stacking (Table 1). In comparison, the frustrated planarity of small donor molecules (D) due to the presence of out-of-plane sidechains, and their electrostatic repulsion due to their electron donating character (Figure 2b), disrupts their tendency to form highly dense packing systems in the solid-state organization. A collection of crystal structures of D molecules organizes as isolated units in 0D herringbone, or with limited co-facial π -stacking like 1D herringbone and slip-stack arrangements (Table 1). This reflects in a broad distribution of high void fraction values, indicating that D molecules form less densely packed crystals.

As for A-D-A molecules, the peculiarity of their molecular shape facilitates different crystallization packing motifs with intermediate voids fractions, enabling the formation of highly interconnected systems like brickwork and reticular shapes that are not observed for D and D-A small molecules. The molecular structure is characterized by a limited flexibility of the backbone which is ensured by lock-in configurations and a high sidechain flexibility around the dihedral angle θ (Figure 2) at the same time.

Noncovalent conformational locks have been shown to be an efficient tool for increasing the electronic conjugation along the backbone due to an enhanced planarity of the π -conjugated system.⁷⁵⁻⁷⁷ In particular, S \cdots O interactions can be enabled between the acceptor groups and the central donor core of A-D-A molecules. Therefore, S \cdots O close contacts ranging from 2.6 Å and 2.8 Å have been found for all the structures available (Figure S2), except for o-IDTBR which contains S \cdots N noncovalent interaction instead, due to its unique chemical design. Similar to the S \cdots O interactions, S \cdots N has also been found to be responsible for a reduced torsional angle between the moieties involved, leading to a more planar configuration of the backbone.⁷⁸ Nevertheless, donor and acceptor units still present a certain degree of flexibility, which plays a role for the adapting capability of the A-D-A molecules to facilitate the molecular organization in solid-state. The overall flexibility of a molecule often enables a high degree of polymorphism and

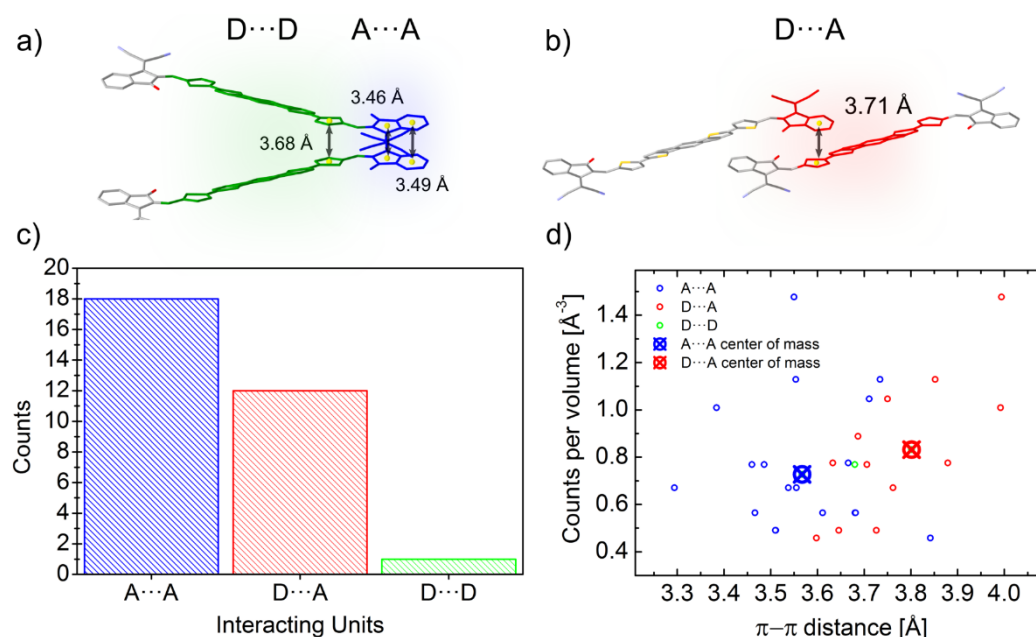


Figure 4 (a) Twisted dimer of an IEICO molecule involving two different close contacts: A...A (highlighted in blue) and D...D (highlighted in green). (b) IEICO coaxial dimer with a D...A close contact highlighted in red. Distances between centroids (yellow spheres) are represented. Side chains and hydrogen atoms have been omitted for clarity (c) Histogram of the different close contacts found in the A-D-A family molecules analysed in the work. (d) Close contacts distribution over the π - π range normalised by the number of counts per volume. Center of mass for the A...A and D...A contact is also plotted in the graph.

conformational polymorphism.⁷⁹ As a result, A-D-A molecules would be expected to have a high likelihood of polymorphism, as reported recently for ITIC⁴¹.

This flexibility reflects in a definite vertical displacement d of the acceptor units with respect to the central part of the backbone (Figure 2b). By analysing the crystal structures of the A-D-A molecules, this distance shows a value distribution ranging from 0 Å (central D unit lying in-plane with respect to the A unit) to about 1.9 Å (backbone with inflection) (Figure S2). Across the series of A-D-A single crystals analysed in this study, we have found that the sidechains project out-of-plane at an angle θ ranging from about 45–70° (Figure S1). The sidechain dihedral angle is broadly distributed around the mean value of 56°, leading to a wide variety of geometrical conformations. Their ability to change orientations indicates that these molecular fragments adapt to facilitate molecular organization. In the reticular packing geometry, for instance, sidechains volumes are protruding perpendicularly from the molecular backbones, pointing towards the central voids created by the reticular space filling (Figure 5). This suggests for the sidechains to be relevant in the formation of this 3D motif, as they occupy the same space region in all the structure with the same arrangement. Therefore, we encourage further studies to be carried out on the optimization of the sidechains in order to achieve systems with high propensity in crystallising in this way, since a proper chemical design can ensure more efficiently the space filling of the reticular lattice central voids.

Intermolecular close-contacts

Besides their contribution to the overall molecular flexibility, the sidechains also exert influence also on the A-D-A intermolecular interactions. We analysed statistically the intermolecular close contacts for a selection of A-D-A crystal structures, by looking at the

centroid-to-centroid distances between aromatic rings within the conjugated donor core (D) and acceptor units (A) as shown in Figure 4a-b. In doing so, we found three different kinds of close contacts according to the specific molecular units involved: A...A, D...A and D...D. We observed that the A units were involved in 26 out of the 27 total close contacts (i.e. their centroid-to-centroid distance d is ≤ 4.0 Å), while only one D...D contact was found. By looking at the distribution of the centroid-to-centroid distances for the contacts found in the crystal structures, it was also possible to analyse in more qualitative terms the two most common contacts configurations (A...A and D...A) by comparing the position of their centre of mass (Figure 4d). This parameter represents the average π - π distance characteristic of a specific contact, calculated by counting its frequency in the unit volume (10^3 Å^3). The non-negligible shift of 0.24 Å between A...A and D...A contacts demonstrates the higher propensity of the acceptor units to be involved in closer contacts. This can be explained as the bulky volume of the sidechains largely precludes co-facial π -stacking between donor cores while favouring interactions between the acceptor units, as predicted by Hou *et al.*¹ Thus, an appropriate design of the electron deficient groups (A units) of the A-D-A molecules is crucial for the molecular organization in the solid-state.

Structure	m_1	m_2	m_3
2D π-π stacking			
IDIC	0.30	>10	0.5
ITN-C9	0.74	>10	2.88
IDIC-4H	4.98	>10	2.46
<i>m</i> -4TICO	0.38	>10	3.83
ITzN-C9	0.37	3.40	1.45
<i>m</i> -ITIC	0.20	0.96	0.69
3D π-π stacking			
ITCT-DM	1.11	1.30	0.38
<i>o</i> -IDTBR	0.32	2.12	3.36
4TIC	0.36	2.41	4.33
IEICO	0.63	1.07	2.38

Table 2 Effective mass values (in free-electron mass m_0 unit) calculated along the three directions defined in Figure 5: d_1 , d_2 and d_3 . Harmonic averages are also shown.

Topological connectivity and charge transport

Reticular lattices result in a superior degree of geometrical connectivity, as compared to any other common packing motif within this class of materials. For example, by observing these structures in the top view (Figure 5) it is clear how reticular lattices show a more complex texture of A-D-A conjugated backbones when compared to brickwork motifs. Theoretical studies on different systems have shown the importance of the topological connectivity towards the achievement of better performing systems in terms of charge transport.¹⁸ Moreover, resistivity measurements performed on functionalized pentacene proved how a precise crystal engineering can drastically enhance the charge transport due to a more functional solid-state organization.¹⁶ One way to estimate the carrier mobility in the solid-state is by calculating the effective mass,

which can be derived from the band structure of the crystal. Moreover, it is well known that this quantity can be obtained along chosen geometric directions, which makes it ideal for the evaluation of the intrinsic anisotropy of materials in terms of charge transport. A similar study has already been successfully performed on molecular crystals.⁸⁰

To this end, we performed DFT calculations to predict the band structure of a number of different A-D-A crystal structures and we explored the effect of the lattice geometry on the electron transport anisotropy. The brickwork ITIC polymorph⁴¹ was excluded from the calculations due to degenerate conduction bands (the energy difference between the first lowest conduction bands was less than 0.025 eV, which is the thermal energy at room temperature). By comparing 2D and 3D packing motifs it was possible to study how the topological connectivity of A-D-A molecules affects the anisotropy of the charge carrier transport.

By assuming the conjugated backbone (D unit) and the acceptors (A units) to be the molecular groups providing the main charge percolation pathways for the charge transport, the 2D structures can be viewed as a sequence of conducting planes extending over the d_1 and d_3 directions and stacking along d_2 (Figure 5a-b). Given the higher geometrical complexity of 3D lattices, we defined d_1 , d_2 and d_3 as in Figure 5a-b. By looking at the curvature of the band structure minima calculated along those three vectors, we found that for 2D structures there is often a very high (>10) electron effective mass along the d_2 direction (see Table 2), whereas the masses along both d_1 and d_3 are generally significantly lower: this implies that the electron mobility is favoured along those directions, but hindered along the stacking d_2 direction. The very low values for the effective masses of ITzN-C9 and *m*-ITIC are most probably due to the smaller stacking distance along d_2 , as compared to the other 2D structures (Figures S3-8). This can open the possibility for the electron transport

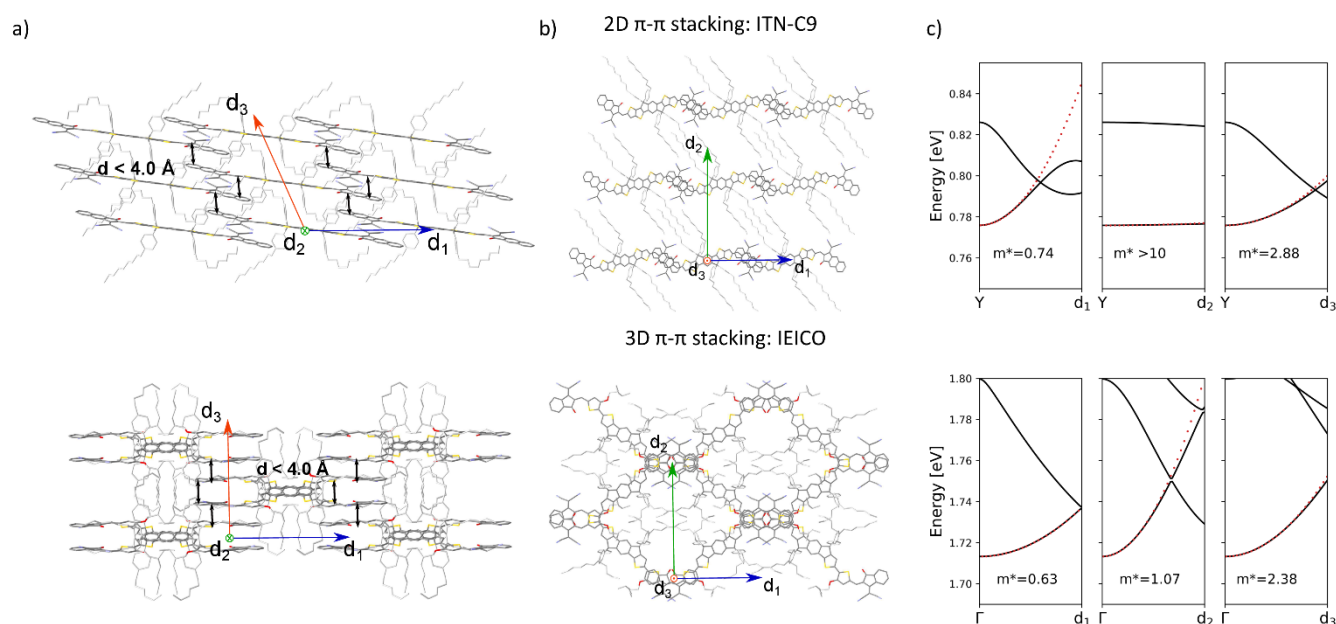


Figure 5 (a) Lateral views of the brickwork 2D packing motif of ITN-C9 (top) and reticular 3D packing of IEICO (bottom). Black arrows represent centroid-to-centroid close contacts ($d < 4.0 \text{ \AA}$) (b) Top views of the packing structures of ITN-C9 (top) and IEICO (bottom) molecules. (c) Calculated conduction band with DFT along d_1 , d_2 and d_3 directions for ITN-C9 (top) and IEICO (bottom), effective mass values are also shown. Solvent molecules and hydrogen atoms have been omitted from panels a-b for clarity.

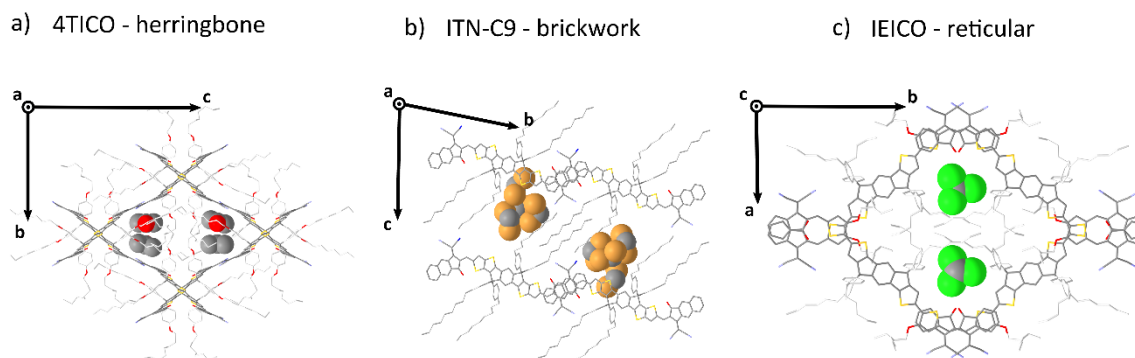


Figure 6 Graphic representation of the three most common molecular packing for A-D-A molecules. A section of the unit cell of 4TICO (a), ITN-C9 (b) and IEICO (c) is shown with their respective solvent inclusions: $\text{C}_3\text{H}_6\text{O}$, CH_2Br_2 and CHCl_3 , which have been highlighted using a space fill model.

to be occurring between adjacent domains. 3D structures are generally characterized by low values along any direction (Figure 5, Table 2 and Figures S9–11). Overall, these results suggest an intrinsic anisotropy in 2D structures, whereas the transport in 3D structures seems to be more isotropic. These calculations provide theoretical justification to the intuitive expectation of charge carrier transport along π -stacking interactions and contacts.

Solvated structures

It is apparent from the known A-D-A crystals that solvates are commonly present in these systems, being understood that solvent inclusions occur for systems with high solvent-solute interactions (i.e. high solubility), but also for the nature of their shape and packing (i.e. minimize frustration).⁸¹ As a proof of concept, 4TIC and 4TICO molecules co-crystallized with antisolvent inclusions of CH_3OH and $\text{C}_3\text{H}_6\text{O}$, respectively (Table 1). The presence of antisolvent inclusions cannot be just explained as a result of a solute-solvent affinity, as they rather provide an efficient void space filling. In-depth analysis of our extensive dataset shows that the solvent molecules preferentially sit in the central voids left by the sidechains away from the backbone, despite the differences in structures and molecular arrangements (Figure 6). By calculating the short contacts involving the guest molecules, we can conclude that non-halogenated solvents have never or barely been found to be in contact with the central backbone, but rather with the sidechains. On the other hand, by increasing the solvent halogenation it becomes more common to observe close contacts which involve solvent and molecular backbone. Finally, only the case of dibromo-methane has strong solvent-solvent interactions, as the $\text{Br}\cdots\text{C}$ distance was found to be 2.52(5) Å ($\text{Br}\cdots\text{C}$ Van der Waals radii sum is 3.55 Å) for ITN-C9 structure (Figure 6b). In this last case, the extensive solvent inclusion accounts for a non-negligible 12.02% increase in the void fraction when the solvent is ignored in the void calculation. In general, this value was found to be higher when halogenated solvent inclusions were found in the crystal structure (Table 1). Following these considerations, the use of non-halogenated solvents and an accurate chemical design of the side chains can help in obtaining solvate-free crystal structures.

Conclusions

By studying the molecular organization of the NFAs in the solid-state it is possible to derive information about the propensity of a material to crystallize and form interconnected domains along different directions, providing efficient channels for the charge percolation. As part of this study, five new molecules were synthesised and crystallized by solvent vapour diffusion, in addition to four new crystal structures of molecules known from literature. Relevant crystal structures from existing literature were also introduced in the study. This extensive dataset was used to analyse the solid-state organization of A-D-A NFAs in comparison with two families of small molecules: D and D-A molecules. We highlighted the trends between them in terms of molecular packing, showing how the peculiar shape of A-D-A NFAs leads to a unique motif as the 3D reticular arrangement. A statistical approach to studying the intermolecular close-contacts revealed the highest propensity of the acceptor groups to be leading the intermolecular network typical of 2D brickwork and 3D reticular packing motifs. Sidechains, being located near the centre of the molecule, act as a steric hindrance for the central part of the backbone, strongly limiting its involvement in intermolecular close contacts.

The impact of crystal packing and topological connectivity on charge transport was explored by DFT calculations. In particular, by predicting the band structure of the A-D-A crystals presented in this work, it was possible to derive the effective mass along different directions in order to estimate the intrinsic electron mobility anisotropy of the molecules. The 3-dimensional domain connectivity, typical of the reticular packing, led to very low values of the effective mass along the different directions, resulting in a more isotropic geometry compared to the other 2D packing motifs. Based on this holistic picture, we encourage the future research to follow up on the study of the NFA crystal engineering, in order to address one of the main obstacles towards large-scale commercialization of OPV devices, i.e. low charge mobility and anisotropic charge transport.

Conflicts of interest

There are no conflicts to declare.

Acknowledgements

P.M. acknowledges Merck Chemicals Ltd. and the European Union's Horizon 2020 research and innovation programme under Marie Skłodowska Curie Grant agreement no. 722651 (SEPOMO) for the support in the realization of this work.

G.B. thanks both Merck and EPSRC for a Ph.D. studentship via the Centre of Doctoral Training (CDT) in Next Generation Computational Modelling (NGCM) (grant no. EP/L015382/1). The calculations were carried out on the Iridis5 Supercomputer of the University of Southampton and on the UK national high-performance computing service, ARCHER, for which access was obtained via the UKCP consortium and funded by EPSRC grant no. EP/P022030/1.

Bibliography

1. J. Hou, O. Inganäs, R. H. Friend and F. Gao, *Nature Materials*, 2018, **17**, 119-128.
2. P. Cheng, G. Li, X. Zhan and Y. Yang, *Nature Photonics*, 2018, **12**, 131-142.
3. C. Yan, S. Barlow, Z. Wang, H. Yan, A. K. Y. Jen, S. R. Marder and X. Zhan, *Nature Reviews Materials*, 2018, **3**, 18003.
4. S. Zhang, Y. Qin, J. Zhu and J. Hou, *Adv Mater*, 2018, **30**, 1800868.
5. H. Zhang, H. Yao, J. Hou, J. Zhu, J. Zhang, W. Li, R. Yu, B. Gao, S. Zhang and J. Hou, *Adv Mater*, 2018, **30**, 1800613.
6. Y. Lin, Z.-G. Zhang, H. Bai, J. Wang, Y. Yao, Y. Li, D. Zhu and X. Zhan, *Energy & Environmental Science*, 2015, **8**, 610-616.
7. J. Yuan, Y. Zhang, L. Zhou, G. Zhang, H.-L. Yip, T.-K. Lau, X. Lu, C. Zhu, H. Peng, P. A. Johnson, M. Leclerc, Y. Cao, J. Ulanski, Y. Li and Y. Zou, *Joule*, 2019, DOI: 10.1016/j.joule.2019.01.004.
8. J. Zhao, Y. Li, G. Yang, K. Jiang, H. Lin, H. Ade, W. Ma and H. Yan, *Nature Energy*, 2016, **1**, 15027.
9. S. Zhang, L. Ye and J. Hou, *Advanced Energy Materials*, 2016, **6**, 1502529.
10. S. Li, W. Liu, C. Z. Li, M. Shi and H. Chen, *Small*, 2017, **13**.
11. D. Qian, Z. Zheng, H. Yao, W. Tress, T. R. Hopper, S. Chen, S. Li, J. Liu, S. Chen, J. Zhang, X. K. Liu, B. Gao, L. Ouyang, Y. Jin, G. Pozina, I. A. Buyanova, W. M. Chen, O. Inganäs, V. Coropceanu, J. L. Bredas, H. Yan, J. Hou, F. Zhang, A. A. Bakulin and F. Gao, *Nat Mater*, 2018, **17**, 703-709.
12. J. Zhang, H. S. Tan, X. Guo, A. Facchetti and H. Yan, *Nature Energy*, 2018, **3**, 720-731.
13. W. Chen and Q. Zhang, *Journal of Materials Chemistry C*, 2017, **5**, 1275-1302.
14. S. Berny, N. Blouin, A. Distler, H. J. Egelhaaf, M. Krompiec, A. Lohr, O. R. Lozman, G. E. Morse, L. Nanson, A. Pron, T. Sauermann, N. Seidler, S. Tierney, P. Tiwana, M. Wagner and H. Wilson, *Adv Sci (Weinh)*, 2016, **3**, 1500342.
15. J.-Y. W. Ze-Fan Yao, and Jian Pei, *Crystal Growth & Design*, 2018, **18**, 7-15.
16. J. S. B. John E. Anthony, David L. Eaton, and S. R. Parkin, *J. Am. Chem. Soc.*, 2001, **123**, 9482-9483.
17. J. B. Sherman, B. Purushothaman, S. R. Parkin, C. Kim, S. Collins, J. Anthony, T.-Q. Nguyen and M. L. Chabiny, *Journal of Materials Chemistry A*, 2015, **3**, 9989-9998.
18. B. B. Thorsten Vehoff, Alessandro Troisi, and Denis Andrienko, *JACS*, 2010, **132**, 11702.
19. L. Ye, X. Jiao, M. Zhou, S. Zhang, H. Yao, W. Zhao, A. Xia, H. Ade and J. Hou, *Adv Mater*, 2015, **27**, 6046-6054.
20. N. A. Ran, S. Roland, J. A. Love, V. Savikhin, C. J. Takacs, Y. T. Fu, H. Li, V. Coropceanu, X. Liu, J. L. Bredas, G. C. Bazan, M. F. Toney, D. Neher and T. Q. Nguyen, *Nat Commun*, 2017, **8**, 79.
21. H. Kang, W. Lee, J. Oh, T. Kim, C. Lee and B. J. Kim, *Acc Chem Res*, 2016, **49**, 2424-2434.
22. G. M. Su, T. V. Pho, N. D. Eisenmenger, C. Wang, F. Wudl, E. J. Kramer and M. L. Chabiny, *J. Mater. Chem. A*, 2014, **2**, 1781-1789.
23. S. Jinnai, Y. Ie, M. Karakawa, T. Aernouts, Y. Nakajima, S. Mori and Y. Aso, *Chemistry of Materials*, 2016, **28**, 1705-1713.
24. C. Wang, H. Dong, L. Jiang and W. Hu, *Chem Soc Rev*, 2018, **47**, 422-500.
25. M. Mas-Torrent and C. Rovira, *Chem Rev*, 2011, **111**, 4833-4856.
26. G. Han, Y. Guo, X. Song, Y. Wang and Y. Yi, *Journal of Materials Chemistry C*, 2017, **5**, 4852-4857.
27. R. Yu, H. Yao, L. Hong, Y. Xu, B. Gao, J. Zhu, Y. Zu and J. Hou, *Advanced Energy Materials*, 2018, DOI: 10.1002/aenm.201802131, 1802131.
28. D. Yan, W. Liu, J. Yao and C. Zhan, *Advanced Energy Materials*, 2018, DOI: 10.1002/aenm.201800204, 1800204.
29. Q. Wu, D. Zhao, M. B. Goldey, A. S. Filatov, V. Sharapov, Y. J. Colon, Z. Cai, W. Chen, J. de Pablo, G. Galli and L. Yu, *ACS Appl Mater Interfaces*, 2018, **10**, 10043-10052.
30. M. Wu, J. Zhou, Y. Luo, N. Zheng, C. Wang, L. Liu, Z. Xie and Y. Ma, *Organic Chemistry Frontiers*, 2018, DOI: 10.1039/c8qo00934a.
31. S. M. Swick, W. Zhu, M. Matta, T. J. Aldrich, A. Harbuzaru, J. T. Lopez Navarrete, R. Ponce Ortiz, K. L. Kohlstedt, G. C. Schatz, A. Facchetti, F. S. Melkonyan and T. J. Marks, *Proc Natl Acad Sci U S A*, 2018, DOI: 10.1073/pnas.1807535115.
32. X. Shi, X. Liao, K. Gao, L. Zuo, J. Chen, J. Zhao, F. Liu, Y. Chen and A. K. Y. Jen, *Advanced Functional Materials*, 2018, DOI: 10.1002/adfm.201802324, 1802324.
33. J. Qu, H. Chen, J. Zhou, H. Lai, T. Liu, P. Chao, D. Li, Z. Xie, F. He and Y. Ma, *ACS Appl Mater Interfaces*, 2018, **10**, 39992-40000.
34. Z. Liang, M. Li, X. Zhang, Q. Wang, Y. Jiang, H. Tian and Y. Geng, *Journal of Materials Chemistry A*, 2018, **6**, 8059-8067.
35. S. Li, L. Ye, W. Zhao, S. Zhang, H. Ade and J. Hou, *Advanced Energy Materials*, 2017, **7**, 1700183.
36. WO 2018/065350.
37. Y. Lin, J. Wang, Z. G. Zhang, H. Bai, Y. Li, D. Zhu and X. Zhan, *Adv Mater*, 2015, **27**, 1170-1174.
38. Y. Yang, Z. G. Zhang, H. Bin, S. Chen, L. Gao, L. Xue, C. Yang and Y. Li, *J Am Chem Soc*, 2016, **138**, 15011-15018.
39. H. Yao, Y. Chen, Y. Qin, R. Yu, Y. Cui, B. Yang, S. Li, K. Zhang and J. Hou, *Adv Mater*, 2016, **28**, 8283-8287.
40. Y. Lin, Q. He, F. Zhao, L. Huo, J. Mai, X. Lu, C. J. Su, T. Li, J. Wang, J. Zhu, Y. Sun, C. Wang and X. Zhan, *J Am Chem Soc*, 2016, **138**, 2973-2976.
41. T. J. Aldrich, M. Matta, W. Zhu, S. M. Swick, C. L. Stern, G. C. Schatz, A. Facchetti, F. S. Melkonyan and T. J. Marks, *J Am Chem Soc*, 2019, DOI: 10.1021/jacs.8b13653.

42. X. Shi, L. Zuo, S. B. Jo, K. Gao, F. Lin, F. Liu and A. K. Y. Jen, *Chemistry of Materials*, 2017, **29**, 8369-8376.
43. H. Burckstummer, E. V. Tulyakova, M. Deppisch, M. R. Lenze, N. M. Kronenberg, M. Gsanger, M. Stolte, K. Meerholz and F. Wurthner, *Angew Chem Int Ed Engl*, 2011, **50**, 11628-11632.
44. A. Arjona-Esteban, J. Krumrain, A. Liess, M. Stolte, L. Huang, D. Schmidt, V. Stepanenko, M. Gsanger, D. Hertel, K. Meerholz and F. Wurthner, *J Am Chem Soc*, 2015, **137**, 13524-13534.
45. M. Planells and N. Robertson, *European Journal of Organic Chemistry*, 2012, **2012**, 4947-4953.
46. S. Wen, Y. Wu, Y. Wang, Y. Li, L. Liu, H. Jiang, Z. Liu and R. Yang, *ChemSusChem*, 2018, **11**, 360-366.
47. B. S. Young, D. T. Chase, J. L. Marshall, C. L. Vonnegut, L. N. Zakharov and M. M. Haley, *Chem Sci*, 2014, **5**, 1008-1014.
48. Z. Xiao, F. Liu, X. Geng, J. Zhang, S. Wang, Y. Xie, Z. Li, H. Yang, Y. Yuan and L. Ding, *Science Bulletin*, 2017, **62**, 1331-1336.
49. T.-C. C. Ken-Tsung Wong, Liang-Chen Chi, Ying-Ying Chu, Akula Balaiah, Shih-Feng Chiu, Yi-Hung Liu, and Yu Wang, *Organic Letters*, 2006, **8**, 5033 - 5036.
50. D. Beaudoin, J. N. Blair-Pereira, S. Langis-Barsetti, T. Maris and J. D. Wuest, *J Org Chem*, 2017, **82**, 8536-8547.
51. Y. Guo, M. Li, Y. Zhou, J. Song, Z. Bo and H. Wang, *Macromolecules*, 2017, **50**, 7984-7992.
52. C. K. Skylaris, P. D. Haynes, A. A. Mostofi and M. C. Payne, *J Chem Phys*, 2005, **122**, 84119.
53. C.-K. Skylaris, A. A. Mostofi, P. D. Haynes, O. Diéguez and M. C. Payne, *Physical Review B*, 2002, **66**.
54. A. A. Mostofi, P. D. Haynes, C.-K. Skylaris and M. C. Payne, *The Journal of Chemical Physics*, 2003, **119**, 8842-8848.
55. S. Holliday, R. S. Ashraf, A. Wadsworth, D. Baran, S. A. Yousaf, C. B. Nielsen, C. H. Tan, S. D. Dimitrov, Z. Shang, N. Gasparini, M. Alamoudi, F. Laquai, C. J. Brabec, A. Salleo, J. R. Durrant and I. McCulloch, *Nat Commun*, 2016, **7**, 11585.
56. K. B. John P. Perdew, Matthias Ernzerhof, *physical review letters*, 1996, **77**.
57. N. D. Hine, *J Phys Condens Matter*, 2017, **29**, 024001.
58. S. Grimme, *J Comput Chem*, 2006, **27**, 1787-1799.
59. L. E. Ratcliff, G. J. Conduit, N. D. M. Hine and P. D. Haynes, *Physical Review B*, 2018, **98**.
60. Y. Hinuma, G. Pizzi, Y. Kumagai, F. Oba and I. Tanaka, *Computational Materials Science*, 2017, **128**, 140-184.
61. *Journal*, 2018, **1.171.39.46**
62. R. C. Hooft, Data collection software; Nonius BV: Delft, The Netherlands, 1998, *Journal*.
63. Z. Otwinowski and W. Minor, in *Methods in enzymology*, Elsevier, 1997, vol. 276, pp. 307-326.
64. B. A. I. M. W. SADABS (Version 2.10), USA, 2003, *Journal*.
65. O. V. Dolomanov, L. J. Bourhis, R. J. Gildea, J. A. Howard and H. Puschmann, *Journal of Applied Crystallography*, 2009, **42**, 339-341.
66. G. M. Sheldrick, *Acta Crystallographica Section C: Structural Chemistry*, 2015, **71**, 3-8.
67. G. R. Desiraju, *Angew Chem Int Ed Engl*, 2007, **46**, 8342-8356.
68. R. Li, W. Hu, Y. Liu and D. Zhu, *Acc Chem Res*, 2010, **43**, 529-540.
69. C. Wang, H. Dong, W. Hu, Y. Liu and D. Zhu, *Chemical Reviews*, 2011, **112**, 2208-2267.
70. C. Wang, H. Dong, H. Li, H. Zhao, Q. Meng and W. Hu, *Crystal Growth & Design*, 2010, **10**, 4155-4160.
71. C. C. Mattheus, G. A. de Wijs, R. A. de Groot and T. T. Palstra, *J Am Chem Soc*, 2003, **125**, 6323-6330.
72. J. Z. Vikram C. Sundar, Vitaly Podzorov, Etienne Menard, Robert L. Willett, Takao Someya, Michael E. Gershenson, John A. Rogers, *Sci Rep*, 2004, **303**.
73. F. Cozzi, S. Bacchi, G. Filippini, T. Pilati and A. Gavezzotti, *Chemistry—A European Journal*, 2007, **13**, 7177-7184.
74. G. E. Morse, I. Gong, Y. Kwar, A. J. Lough and T. P. Bender, *Crystal Growth & Design*, 2014, **14**, 2138-2147.
75. H. Huang, L. Yang, A. Facchetti and T. J. Marks, *Chem Rev*, 2017, **117**, 10291-10318.
76. N. E. Jackson, B. M. Savoie, K. L. Kohlstedt, M. Olvera de la Cruz, G. C. Schatz, L. X. Chen and M. A. Ratner, *J Am Chem Soc*, 2013, **135**, 10475-10483.
77. A. Mahmood, A. Tang, X. Wang and E. Zhou, *Phys Chem Chem Phys*, 2019, DOI: 10.1039/c8cp05763j.
78. G. C. Welch, L. A. Perez, C. V. Hoven, Y. Zhang, X.-D. Dang, A. Sharenko, M. F. Toney, E. J. Kramer, T.-Q. Nguyen and G. C. Bazan, *Journal of Materials Chemistry*, 2011, **21**, 12700.
79. S. M. R.-E. Lian Yu, and Christine A. Mitchell, *Organic Process Research & Development*, 2000, **4**, 396-402.
80. A. M. Silva, B. P. Silva, F. A. M. Sales, V. N. Freire, E. Moreira, U. L. Fulco, E. L. Albuquerque, F. F. Maia and E. W. S. Caetano, *Physical Review B*, 2012, **86**.
81. S. Boothroyd, A. Kerridge, A. Broo, D. Buttar and J. Anwar, *Crystal Growth & Design*, 2018, **18**, 1903-1908.